



### Experimental deformation analysis of an adhesively bonded multi-material joint for marine applications

Journal:	<i>Strain</i>
Manuscript ID	STRAIN-1754.R1
Manuscript Type:	Research Article
Date Submitted by the Author:	06-Jan-2023
Complete List of Authors:	Jaiswal, pankaj; Ghent University Faculty of Engineering and Architecture, Department of Electromechanical, Systems and Metal Engineering Iyer Kumar, Rahul; Ghent University Faculty of Engineering and Architecture, Soete Laboratory, Department of Electromechanical, Systems and Metal Engineering (EMSME) Juwet, Thibault ; Com&Sens Bvba, Com&Sens Bvba Luyckx, Geert ; Com&Sens Bvba, Com&Sens Bvba Cedric, Verhaeghe ; Damen Schelde Naval Shipbuilding, Damen Schelde Naval Shipbuilding De Waele, Wim; Ghent University Faculty of Engineering and Architecture, Soete Laboratory, Department of Electromechanical, Systems and Metal Engineering (EMSME)
Keywords:	MMA adhesive, multi-material joint, strain, digital image correlation, fibre optic sensor

**Experimental deformation analysis of an adhesively bonded multi-material joint for marine applications**

Pankaj R. Jaiswal<sup>1</sup>, R.Iyer Kumar<sup>1</sup>, Thibault Juwet<sup>2</sup>, Geert Luyckx<sup>2</sup>, Cedric Verhaeghe<sup>3</sup>, Wim De Waele<sup>1</sup>

<sup>1</sup>Soete Laboratory, Department of Electromechanical, Systems and Metal Engineering (EMSME), Ghent University, Belgium.

<sup>2</sup> Com&Sens Bvba, Belgium.

<sup>3</sup>Damen Schelde Naval Shipbuilding, The Netherlands.

Emails : [pankajaiswal2007@gmail.com](mailto:pankajaiswal2007@gmail.com)<sup>1</sup>; [rahul.iyerkumar@ugent.be](mailto:rahul.iyerkumar@ugent.be)<sup>1</sup>; [tjuwet@com-sens.eu](mailto:tjuwet@com-sens.eu)<sup>2</sup>; [gluyckx@com-sens.eu](mailto:gluyckx@com-sens.eu)<sup>2</sup>; [C.Verhaeghe@damennaval.com](mailto:C.Verhaeghe@damennaval.com)<sup>3</sup>; [wim.dewaele@ugent.be](mailto:wim.dewaele@ugent.be)<sup>1</sup>.

**Abstract:**

The strength and deformation of full-scale adhesively bonded multi-material joints is studied in this paper. Four joints with a thick layer of Methyl Methacrylate adhesive (MMA) have been manufactured in shipyard conditions. In two specimens, cracks have been introduced at steel-adhesive and composite-adhesive interfaces. One cracked and one un-cracked specimen were subjected to quasi-static tensile testing; the two remaining specimens were stepwise loaded/unloaded with increasing load until failure. The strain in the adhesive layers was measured with digital image correlation (DIC). This showed a predominant shear deformation and dissimilar shear strain patterns for different bond lines. Fibre Bragg (FBG) sensors were used to monitor strains at steel and composite constituents and to detect the onset and evolution of damage in the un-cracked specimen. Strains measured by FBG sensors correspond well with DIC results at nearby regions. All specimens failed by delamination of the composite panel near the composite-adhesive interface.

**Keywords:** MMA adhesive, multi-material joint, strain, digital image correlation, fibre optic sensor.

## 1. Introduction

The soaring demand of durable, robust and lightweight water vehicles has increased the interest in adhesively bonded joints for superstructure assembly to steel hull. The use of structural adhesive and composites in the superstructure has the potential to reduce its weight by about 50 % (1). This enables a significant reduction in fuel consumption and emissions from the ship (1,2). Adhesive bonding is a popular technique for joining dissimilar materials, that further comes with the advantage of low-stress concentration in parent materials compared to traditional joining techniques (welding, riveting and bolting). The strain distribution in an adhesively bonded structure mainly relates to the adhesive layer thickness (3–11), overlap length (12,13), global geometry (14–18), adherend thickness (19), type of adhesive and adherend (6,9,20,21), surface treatment of adherend (22–26) and bond quality. The strain is usually higher at the edges of the joint due to stress concentration (27). Experimental testing of the adhesive joint is the best practice to evaluate and understand the strain development in the adhesive (28). Strain measurement in adhesive bonded joints for watercraft industries is challenging and can be addressed by using non-contact deformation or strain measurement techniques, which allow to evaluate the actual strain on the adhesive.

DIC has demonstrated its excellent potential for strain evaluation in adhesive bond lines (29–32). Angelopoulos (33) determined void content and distribution in large-scale steel/composite adhesive joints based on the local strain evolution characterised using DIC. Saleh et al. (34) implemented DIC to evaluate the full-field strain maps and in-plane deformation in steel/CFRP adhesive joints bonded with a thick layer of MMA adhesive. Askarinejad et al. (35) successfully applied DIC to measure mode II crack initiation and growth in Thick Adherend Shear Test

specimens with an MMA adhesive layer. Likewise, Thäsler et al. (36) suggested a method to monitor and trace the crack in dynamically loaded single lap shear, double lap shear and crack lap shear specimens using 2D DIC. Jaiswal et al. (37) applied DIC to evaluate the deformation of single and double lap specimens with thick layers of MMA adhesive subjected to fatigue loading.

Another technique that has been increasingly used in monitoring of engineering structures is the use of optical fibres with Bragg grating sensor, so-called FBGs. These provide following advantages: up to dozens of sensors in one single fibre, ultrathin and lightweight, electromagnetic immune, safe in explosive and high radiation environments. Embedding FBGs in adhesive is challenging because fibres can break or misalign during manufacturing, and embedded sensors can also lead to a decrease in the strength of the adhesive joint (38). FBG sensors can also be bonded to the outer surface of the constituents of an adhesive joint. Ning et al. (39) measured the dynamic strain distribution during fatigue testing of CFRP/CFRP epoxy-bonded single lap specimens by means of an FBG sensor embedded into the adhesive at the substrate interface. Xavier et al. (40) used DIC and an embedded FBG sensor to measure external and internal strain in the epoxy adhesive of wooden double cantilever beam specimens. Saha and Sullivan (41) recorded the longitudinal surface strain distribution for a composite double lap shear joint subjected to a tension test, by means of embedded FBG sensors (at adhesive-adherend interface and in the bulk adhesive) and DIC. Manterola et al. (42) monitored mode I crack growth in double cantilever beam specimens bonded with rigid methacrylate adhesive and silicone-based flexible adhesive using embedded FBG sensors, DIC, back face strain gauges, ultrasonic inspection and acoustic emission sensors. Jaiswal et al. (43) used FBG and DIC to evaluate the global deformation and local strain distributions in a tensile loaded large-scale joint of a steel bracket and a sandwich panel bonded with thick MMA adhesive. Several FBG sensors were bonded to the outer surfaces of steel and composite panel to monitor

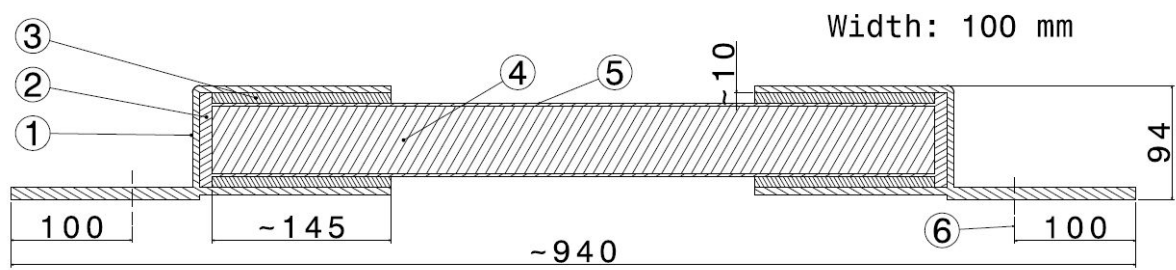
the longitudinal strain during the test; DIC was used to monitor strain in the adhesive bond lines. The use of a glass fibre reinforced superstructure combined with the conventional steel hull is not new in naval industries and several joint designs have been proposed (44). However, the use of fibre reinforced plastics has dramatically reduced in vessel design due to rising challenges in joining the polymer composites to metals (45). CFRP is nowadays preferred over GFRP because of its higher specific strength allowing a lower weight design (46). The present work emphasises on a specific joint design that includes a sandwich structure, formed by CFRP panels and balsa core, that is bonded to a steel flange using a thick MMA structural adhesive. The focus is on the evaluation of global deformation and local strain in the multi-material adhesive joint using FBG sensors and DIC, respectively, during quasi-static tensile testing. The damage mechanisms of the multi-material specimens are evaluated by visual inspection.

This work is part of the Qualify project to develop qualification guidelines for real scale adhesive joints for lightweight and safe maritime transport, funded by Interreg2Seas Mers Zeeën.

## 2. Materials and specimens

The shipbuilding and repair quality standard IACS 47 was used to manufacture a large-scale panel by bonding a sandwich panel (CFRP sheets and balsa wood core) to steel flanges with a thick layer of MMA adhesive in shipyard conditions (47). The sandwich panel represents the superstructure and the steel flange represents the hull of the ship. A high strength shipbuilding structural steel grade AH 36 with 6 mm thickness was used. Four specimens with a width of 100 mm were sectioned by water jet cutting from the large hybrid panel. Two out of four specimens, FsC-1 and FsC-2, had a crack-like flaw introduced at the steel-adhesive interface on one end of the specimen and at the composite-adhesive interface on the other end. The approximately 30 mm long artificial defects were created during the manufacturing stage by

placing thin Teflon sheet inserts at these interfaces before applying the adhesive. The purpose hereof was to study the tolerance of the large-scale adhesive joint to potential manufacturing defects such as kissing bonds. The two other specimens, Fs-1 and Fs-2, were kept intact. The structure, geometry and dimensions of the un-cracked and cracked specimen are shown in Figure 1 (a), (b) and (c), respectively. The bond line thicknesses of the sectioned specimens were found to vary from 7 to 10 mm, which is a normal consequence of the shipyard manufacturing constraints.



(a)

[1:Steel, 2:Foam, 3: Adhesive, 4: Balsa core, 5: Composite, 6: Grip length]



(b)

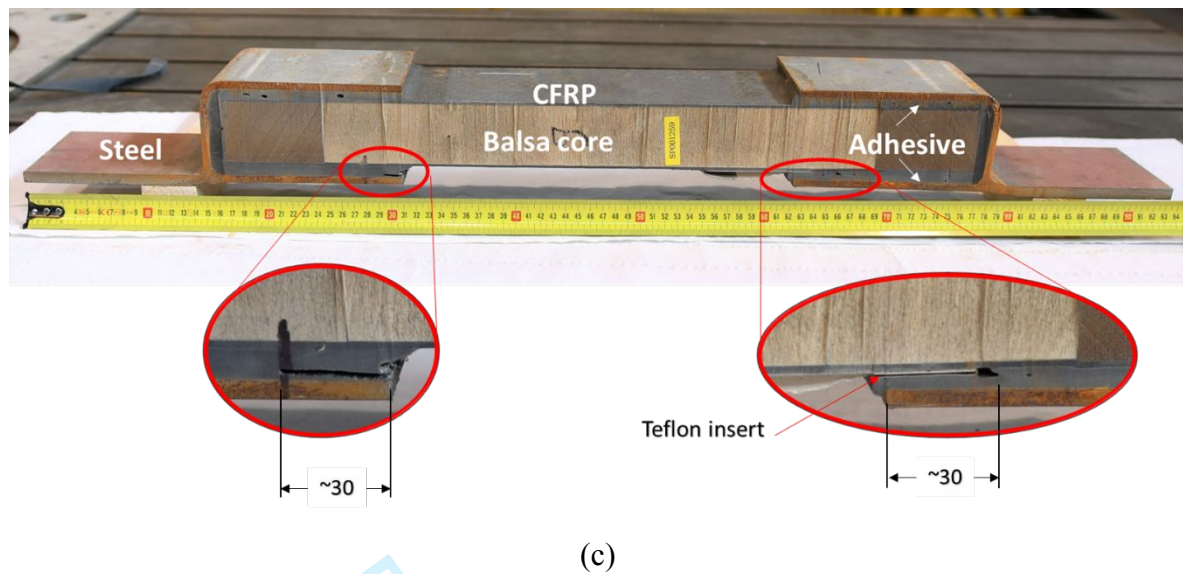


Figure 1 Schematic illustration (a) and the actual appearance of fabricated large scale un-cracked (b) and cracked (c) adhesive joint (all dimensions in mm).

A two-component MMA adhesive has been selected because of its high strength to weight ratio and ductility, which are essential characteristics for the use of adhesive joints in shipbuilding industries (2). This adhesive needs at least 24 hours of curing at room temperature to reach 100 % of its shear strength. All specimens were tested several weeks following manufacture, thus ensuring full curing of the adhesive. The primary mechanical properties of all constituents are listed in Table 1.

Table 1 Mechanical properties (37,52).

	Steel AH-36	MMA adhesive	CFRP	Balsa
Tensile strength (MPa)	400-500	12-15	600-700	5-10
Yield stress (MPa)	355	-	(brittle failure)	
Young's modulus (GPa)	210	0.207-0.276	36	0.279
Poisson's ratio	0.26	-	0.32	
Lap shear strength (MPa)	-	16-19	-	
Shear modulus (GPa)	-	-	13.7	0.187



1

2

3

4

5

6

7

8

9

10

11

12

13

14

15

16

17

18

19

20

21

22

23

24

25

26

27

28

29

30

31

32

33

34

35

36

37

38

39

40

41

42

43

44

45

46

47

48

49

50

51

52

53

54

55

56

57

58

59

60

### 3. Experiments

Figure 2 shows a schematic diagram of the test setup that consists of a servo-hydraulic testing machine MTS 810, DIC instrumentation, digital single-lens reflex (DSLR) camera and FBG sensor readout system. The MTS 810 has a load cell capacity of 1000 kN and load versus crosshead displacement data was recorded at 5 Hz. The deformation and strains of the adhesive bond lines at the bottom part of the joint are obtained by post-processing images captured by DIC during testing. A DSLR camera is used to monitor the damage in the loaded specimens.

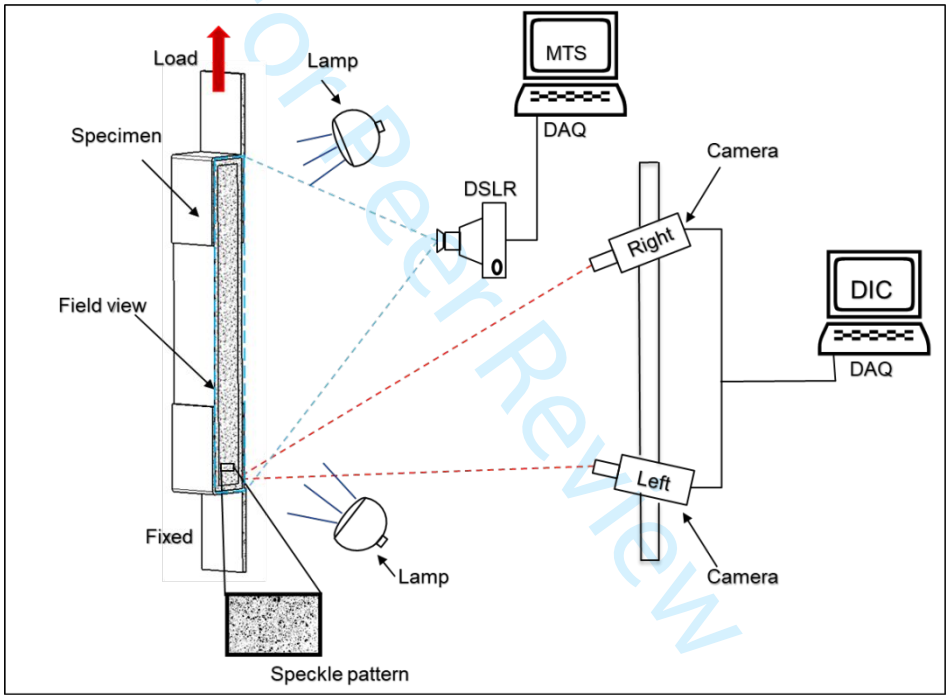


Figure 2 Schematic representation of tensile test setup, including DIC and DSLR camera.

The DIC setup consists of two 5 MPixel monochromatic cameras having a resolution of 14 bits, supplemented with Ricoh 70 mm long lenses and two lamps of 20 W capacity. An acrylic matte white paint is applied over the specimen's surface area of interest to obtain optimal contrast with the black speckle pattern. An optimal speckle size of 0.92 mm was determined based on the area of interest of the specimen. Vic-Snap 9 software (Correlated Solutions inc.) is used to capture synchronised images at a rate of 5 pictures per second during tensile loading of the



specimen. A subset size of 27 x 27 pixels and a step size of 7 pixels were selected for post-processing images in VIC-3D 9 software.

FBG sensors have been mounted on the front and backside of one specimen. Depending on the FBGs' grating period, light with a specific wavelength is reflected. When the fibre is being elongated, a positive Bragg peak shift is induced, and the shift in reflected wavelength can then be used to calculate the strain:

$$\epsilon = \frac{1}{k} \ln \frac{\lambda}{\lambda_0}$$

With  $\lambda$  the wavelength,  $\lambda_0$  the wavelength at the start of the measurements and a calibration factor  $k = 0.776 \times 10^{-6}$ . Two sensor lines containing respectively 12 and 14 FBG sensors with 1 cm spacing were used. The optical fibre was reinforced with 2 rovings of TEX600 glass fibre in a pultrusion process resulting in a strip of approximately 5 mm wide and 1 mm thick. The 2 lines were placed on flanges of the upper and lower steel brackets. In addition, 6 reference FBGs were placed, i.e. 2 on the composite parts and 4 on the steel flanges. The FBGs were read out at 200 Hz using an interrogator 804D (FBGS) with 4 channels.

Initially, quasi-static tensile tests up to failure are conducted on one cracked (FsC-1) and one un-cracked (Fs-1) specimen. Tests are performed at room temperature and a constant cross-head displacement rate of 1 mm/min. The other specimens (i.e., Fs-2 and FsC-2) are subjected to stepwise loading/unloading tensile tests with a load increase of 15 kN in each step until failure, as depicted in Figure 3. These tests are performed in force control mode with a load rate of 15 kN/min. The steel flanges are fixed in hydraulic clamps.

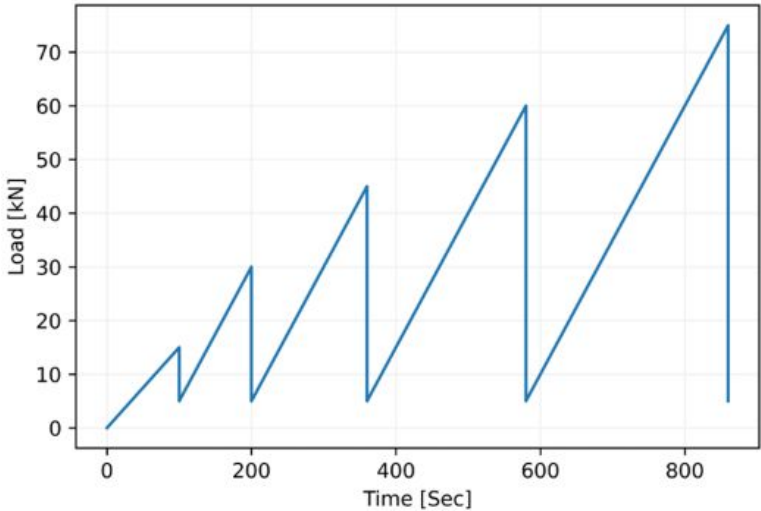


Figure 3 Scheme for stepwise loading/unloading tensile test.

4. Results and discussion

Figure 4 depicts the load versus crosshead displacement curves of all experiments. Both curves of the quasi-static tensile tests present a close to linear behaviour from the start of the test until elastic failure of the specimen. The curves of the stepwise loading/unloading tests show hysteresis in the mechanical response. The unloading curves do not follow the same trajectory of the loading curves (close to linear) since mechanical energy is being dissipated. The uncracked specimens (i.e., Fs-1 and Fs-2) demonstrated higher stiffness (ratio of load over extension) than the cracked specimens (i.e., FsC-1 and FsC-2) in both types of test. In 3 out of 4 tests, failure occurred by CFRP delamination (see further) at an almost identical maximum load (76.5kN, 79.7kN and 78.7kN for specimens Fs-1, FsC-1 and Fs-2 respectively). The cracked specimen tested in stepwise loading mode (FsC-2) failed at a higher force, i.e. 89.6 kN

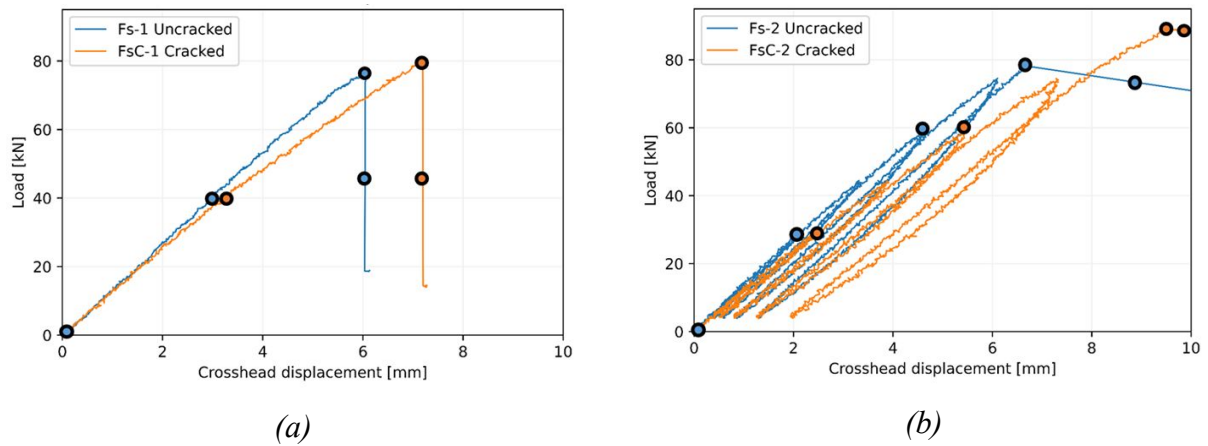


Figure 4 Mechanical behaviour of large scale specimens subjected to quasi-static tensile testing: (a) monotonically loaded, (b) stepwise loaded/unloaded. The circles refer to load levels used in the next figure.

#### 4.1 Characterisation of strain evolution

The strain distribution in the adhesive is obtained by the DIC technique introduced above. Figure 5 and Figure 6 present surface distributions of in-plane shear strain ( $\epsilon_{xy}$ ) at the lower joints of all specimens at various load levels indicated in Figure 4 Mechanical behaviour of large scale specimens subjected to quasi-static tensile testing: (a) monotonically loaded, (b) stepwise loaded/unloaded. The circles refer to load levels used in the next figure. Figure 4. The strain distribution pattern in the bond lines at both sides of the specimen are similar for monotonic and stepwise loaded specimens. Naturally, a general trend of increasing shear strain with increasing load can be observed in all tests.

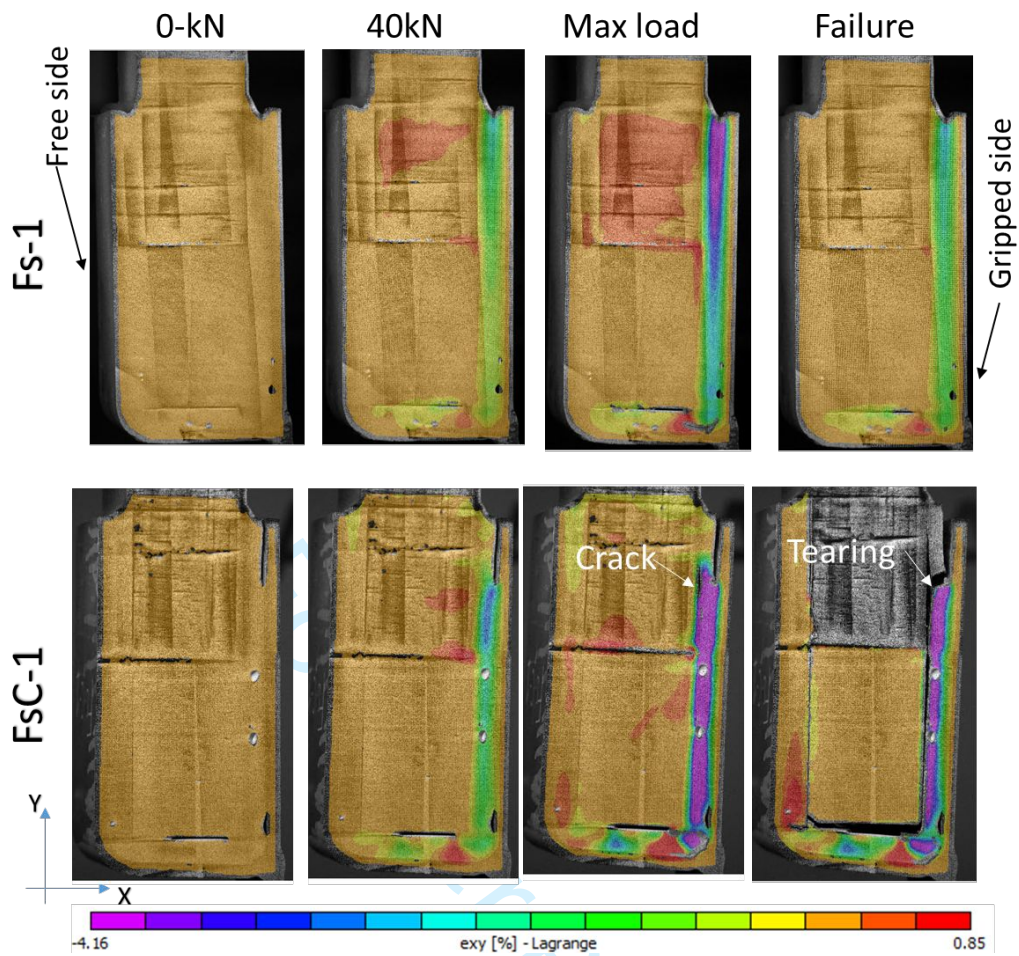


Figure 5 Shear strain ( $\epsilon_{xy}$ ) distributions at the lower joint of the un-cracked (Fs-1) and the cracked ( FSC-1) specimens at different load levels during the quasi-static tensile test.

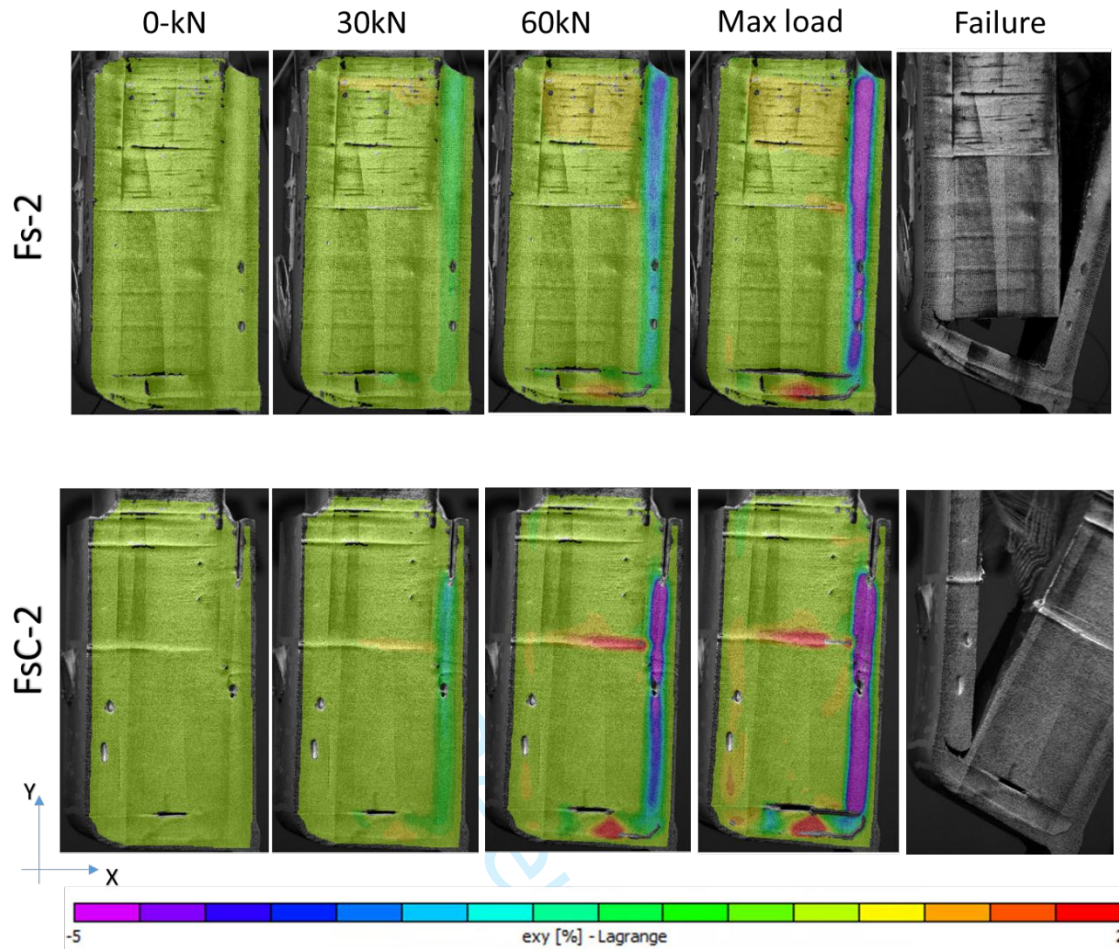


Figure 6 Shear strain ( $\epsilon_{xy}$ ) distributions at the lower joint of the un-cracked (Fs-2) and the cracked (FsC-2) specimens at different load levels during the stepwise tensile test.

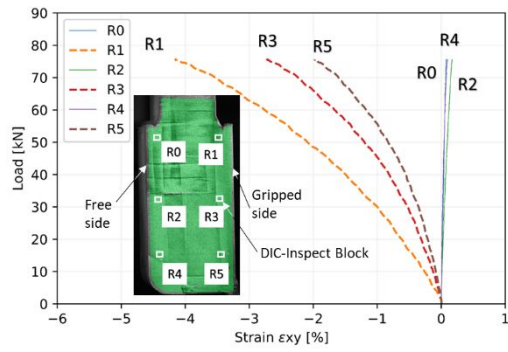
The first image in every row of the above figures is the reference image captured just before the start of the test and hence refers to zero strain. At a load level of 40 kN during the quasi-static tensile test (second column in Figure 5), the bond line at the gripped side of the joint shows significant strain development with maximum values occurring at the centre of the bond line. Similar observations can be made for the 30 and 60 kN load levels in the cyclic tensile test (Figure 6). At the maximum load, the gap between balsa and the bottom of the steel profile increases and the magnitude of the shear strain decreases from top to bottom of the bond line. Simultaneously, minor damage has initiated at the adhesive-composite interface at the gripped side of specimens FsC-1 and Fs-2. Eventually, the last images show the tearing of the adhesive



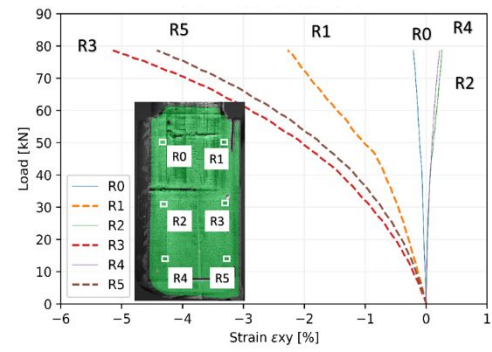
at specimen FsC-1 and delamination of the composite near the adhesive-composite interface was observed in all specimens. For specimen Fs-1, failure occurred at the side of the component that was not monitored by DIC. The shear strain distribution in the bond line at the free side of the joint remains almost negligible throughout the test. Due to transverse asymmetry and thus load eccentricity in the specimens, higher strain values occurred at the gripped side of the specimen. A similar analysis of peel and longitudinal strain distributions allows to conclude that the adhesive at the gripped side is predominantly loaded in shear mode.

The observed non-homogeneous strain distribution has also been reported by Saleh et al. (34) who studied the strain distribution in a double lap adhesive joint subjected to tensile load. The double lap joints consisted of steel adherends bonded to two CFRP straps using both epoxy and MMA based adhesive with a thickness of 8 mm. DIC measurements revealed that the shear strain distribution along the bondline was highly non-uniform and FEM results showed that the highest peel stresses occur at the centre of the specimen (i.e., at the discontinuity between steel adherends).

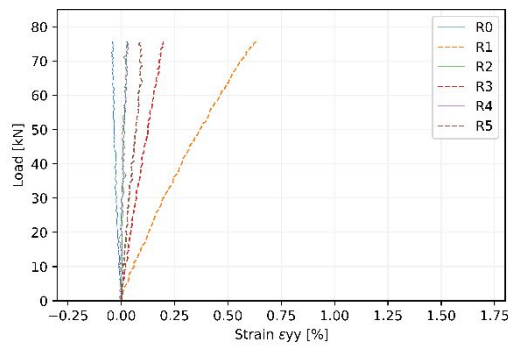
Figure 7 shows shear, longitudinal and peel strain distributions at different locations in the adhesive for specimens Fs-1 and FsC-1. Similarly, Figure 8 presents local strain plots for specimens Fs-2 and FsC-2. Six different regions (i.e. R0 to R5) were defined at the adhesive surface to calculate and plot the average strain in these regions till maximum load. Comparing the strain values obtained for cracked and un-cracked specimens respectively, an almost similar order of strain magnitude is found, both at the gripped and free sides of the joints.



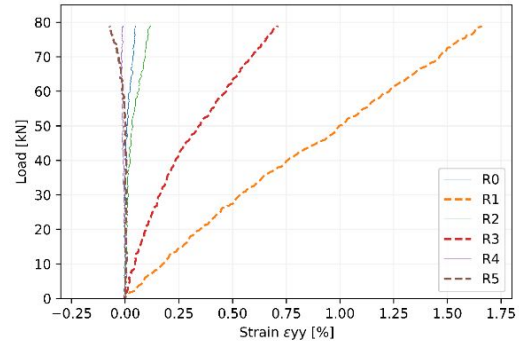
(a) shear strain



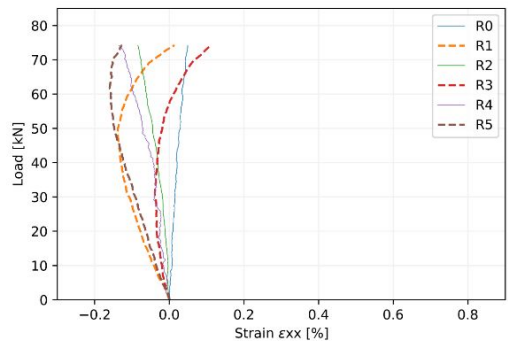
(b) shear strain



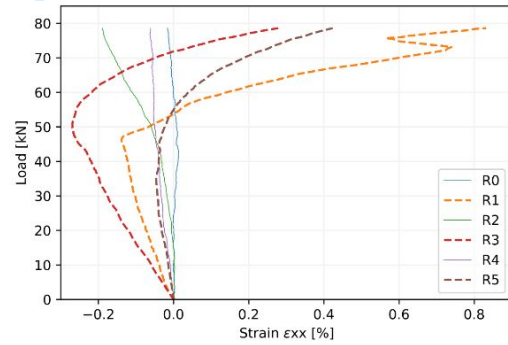
(c) longitudinal strain



(d) longitudinal strain



(e) peel strain



(f) peel strain

Figure 7 Load versus local strain plots for six different regions at the adhesive surface of un-cracked (Fs-1; a,c,e) and cracked (FsC-1; b,d,f) specimens subjected to monotonic tensile load. R0 to R5 refer to DIC inspection blocks.



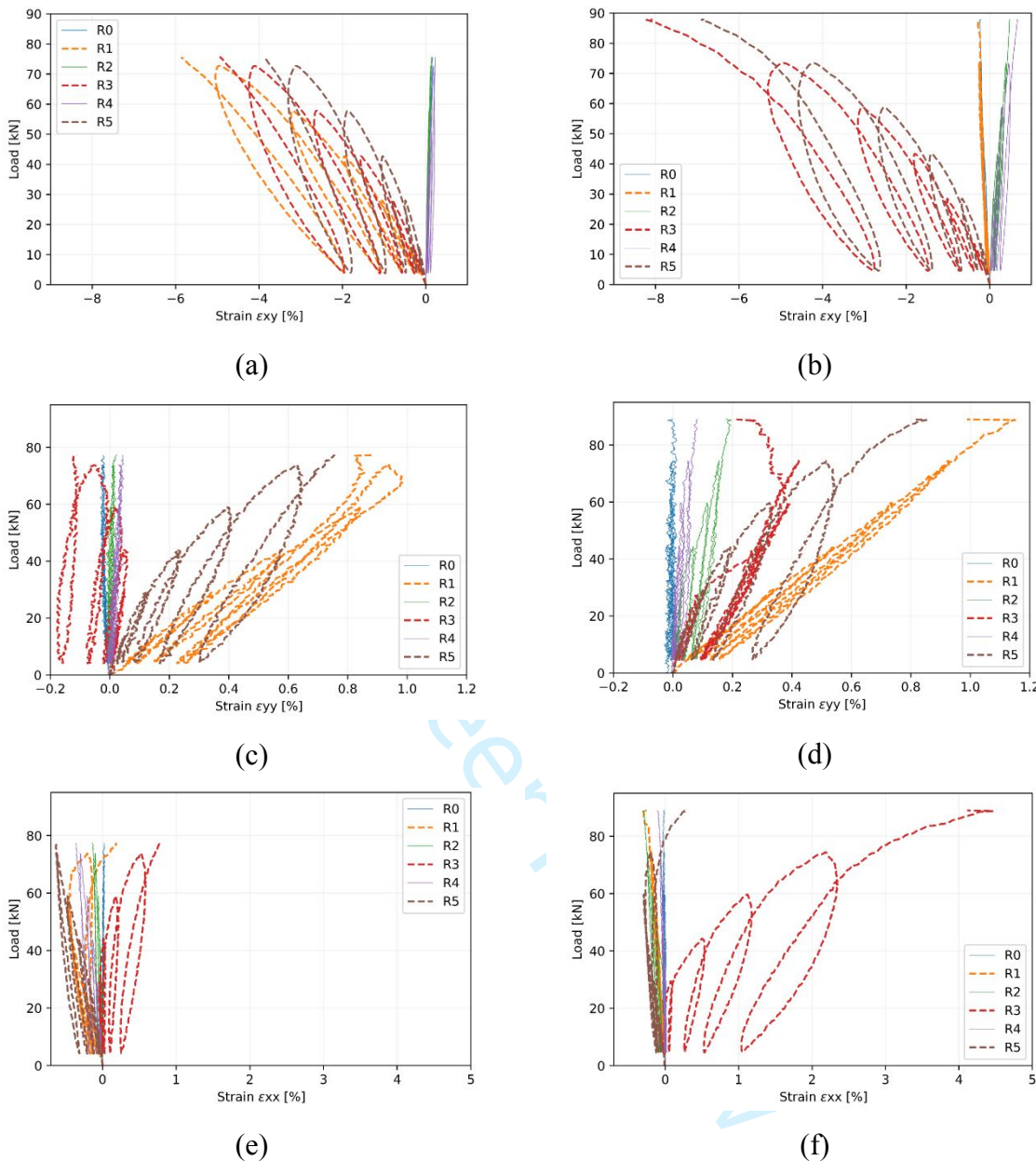


Figure 8 Load versus local strain plots for six different regions at the adhesive surface of un-cracked (Fs-2; a,c,e) and cracked (FsC-2; b,d,f) specimens subjected to stepwise loading/unloading tensile load ( shear strain a,b; normal c,d; peel strain e,f). R0 to R5 refer to DIC inspection blocks.

Analysing Figure 7 and Figure 8, it is apparent that all failure strain values are considerably higher at the gripped side of the specimen as compared to its free side. The shear, longitudinal and peel strain in the adhesive at the free side of the joints have an almost negligible magnitude. This shows, not unexpectedly, that the maximum percentage of tensile load is carried by the gripped side of the specimen. The distributions of shear, longitudinal and peel strain at the gripped side of each specimen are similar but not identical. The strain value decreases from top

to bottom of the bond line; inspection blocks R1 and R3 showed higher strain magnitude in each plot of load versus local strain. This observation is attributed to two different reasons. First, the closer proximity of regions R1 and R3 to the stress concentration zone of the joint, and second the bending of the specimen during testing as a result of the joint asymmetry. This bending phenomenon is also visible in the evolution of peel strain shown in Figure 7 (e and f) and Figure 8 (e and f). The curves display a linear evolution of compressive strain until a load of ~50 kN after which they significantly diverge from a linear evolution due to bending of the specimen.

#### ***4.2 FBG measurement of (longitudinal) strain***

Figure 9 shows a schematic diagram and photographs of the un-cracked specimen (Fs-2) instrumented with 32 FBG sensors that measure longitudinal strain (in the direction of the applied load). Twenty-nine sensors are bonded to the front face (i.e., S1 to S26 and S31 to S33) and three sensors are bonded to the back face (i.e., S2-1 to S2-3) of the specimen. Sensors S1 to S13 and S13 to S26 are placed at a pitch distance of 1 cm on the top and bottom steel brackets respectively. Likewise, two sensors (S31, S33) are installed on the flange and two sensors (S2-2, S3-2) on the composite skin of the sandwich panel. DIC inspection blocks with reference S22R3, S32R2, S23R1 and S20R0 are defined at the side of the specimen and on the composite (near the beginning of the bond) and at the centre of the steel flange adjacent to the bond, which are close to the positions of FBG sensors S2-2, S3-2, S23 and S20 respectively. The length and centre distance between DIC inspection blocks have been defined to be nearly the same as for the FBG sensors.; they also report longitudinal strain. Their close proximity to the edges will have a negative influence on the measurement quality but they merely serve as benchmark for the FBGs.



(a)



Figure 10 Load versus longitudinal strain curves for FBG sensors (a) S2-2, S3-2 and S31, (b) S1 to S13 and S2 and (d) S14 to S26 and S2-3.

Figure 10 displays the evolution of longitudinal strain during stepwise loading for each FBG sensor. At the beginning of the test, the strain data was not recorded properly due to technical difficulties in the FBG data acquisition system; hence only the strain values starting from a load of 40 kN are reported. In Figure 10 (a), the sensor mounted on the composite sheet (S3-2) i.e. at the free side of the joint, shows significantly high tensile strain values, while the sensor mounted on the gripped side of the composite (S2-2) shows a negligible compressive strain evolution. This observation is again attributed to the bending of the gripped side specimen during the test and confirmed earlier in Figure 8 (e). As a result, the sensor S3-1 mounted on the steel flange exhibited significant compressive strain values. The sensor S33 failed during the test; hence the strain response is not presented in Figure 10 (a). The strain responses of FBG sensors applied on the steel bracket at the top of the front, and back faces of the specimen (S1 to S13) show a stable, increasing evolution during the first two load blocks (45kN and 60kN). After that, the strain values significantly decrease till failure load; see Figure 10 (b). This strain evolution of sensors S1 to S13 can be directly related to their proximity to the location of internal damage at the gripped side of the lower joint of the specimen just before failure. Since sensors S1 to S5 are close to the damaged region of the joint, strain values dropped significantly due to loss of load transfer during the 75 kN load block. In contrast, sensors S6 to S10 showed stable, increasing evolution due to their distant location from the damage and bending zone of the joint. Sensor S13 is positioned close to the connection between steel flange and steel bracket where significant bending takes place. Therefore, it shows considerable compressive strain compared to sensors S11 and S12. Sensor S2-1 showed negligible strain during the entire test since it is positioned on the non damaged (free) side of the joint.

A similar type of joint has been tensile tested in (43), but using a limited number of FBG sensors for deformation measurements and using acoustic emission sensors for direct damage detection. In this work, the number of FBG sensors has been significantly increased to evaluate the

feasibility of deformation measurements for an indirect assessment of damage. The above discussion indeed demonstrates that the applied configuration of installed FBGs also allows to detect changes in the adhesive bond due to the occurrence of damage. Therefore, FBG sensors can be considered as key instrumentation for a ship joint monitoring system, not only focussing on deformation measurements (53,54) but also monitoring structural health of critical joints.

Unaffected strain evolutions can be observed for sensors S14 to S26 and S2-3, which are placed at the lower side of the joint; see Figure 10 (c). The strain magnitudes measured by these sensors are less than 500 microstrain due to elastic deformation of the steel flange during the tensile test. The FBG sensors allow to accurately measure these small to very small elastic strains.

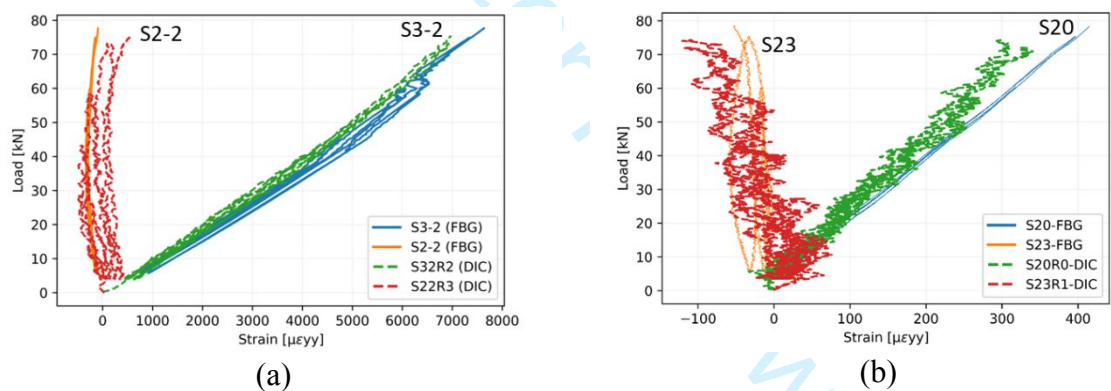


Figure 11 Load versus longitudinal strain curve for FBG sensors and DIC inspection blocks placed on (a) composite and (b) steel.

Turning to the comparison of DIC and FBG measurements, Figure 11 (a) and (b) shows the evolution of longitudinal strain obtained from FBG sensors and DIC inspection blocks located on the composite skin and steel surface adjacent to the adhesive. The results show functional coherence between both types of measurements, in line with the observations reported in (41) for composite joints and in (43) for multi-material joints.

The difference in strain magnitude measured on composite and steel using DIC and recorded by FBG sensors at the gripped side of the specimen is limited to around 10% and 20 %

1  
2  
3 respectively (see Figure 11 (a) and (b)). The relative differences between DIC and FBG data  
4  
5 for composite and steel at the opposite side of the specimen are significantly higher, which is  
6  
7 attributed to the fact that DIC measurements are less accurate at those low strain values. The  
8  
9 results display a linear strain evolution during the loading part of the curve in the cyclic tensile  
10  
11 test, as expected from the load versus displacement plot in Figure 4 (b). The high dispersion  
12  
13 visible in the DIC values is since shallow elastic strain values in composite and steel are  
14  
15 evaluated. The quality of the FBG sensor values is very high, also at low strain values.  
16  
17  
18  
19

## 20 21 **5. Damage characterisation**

22  
23  
24 All specimens showed sudden failure at maximum load, without any warning prior to failure.  
25  
26 A number of images captured by DSLR cameras during the tensile test on specimen Fs-1  
27  
28 illustrate the global bending and sudden failure at four different moments, see Figure 12.  
29  
30

31  
32 Figure 13 shows photographs of failed un-cracked and cracked specimens. The failure modes  
33  
34 of each specimen can be clearly observed visually. As discussed above, load eccentricity due  
35  
36 to joint asymmetry has led to stress concentration at the gripped sides of the specimens. Hence  
37  
38 failure occurred at that side near the adhesive-composite interface. At maximum load,  
39  
40 delamination (or interfacial failure) of the composite panel was observed. This damage also led  
41  
42 to reinforced fibres peeling off, as indicated by the green box in  
43  
44  
45

46  
47 Figure 13. Similar failure phenomena in large scale joints have been reported in (44,55). In all  
48  
49 cases, no failure was observed at the interface between steel and adhesive, nor within the  
50  
51 adhesive itself (44,55).  
52  
53  
54  
55  
56  
57  
58  
59  
60





Figure 12 Photographs illustrating global bending and sudden failure of an un-cracked specimen (Fs-1) at different load levels during the static tensile test.

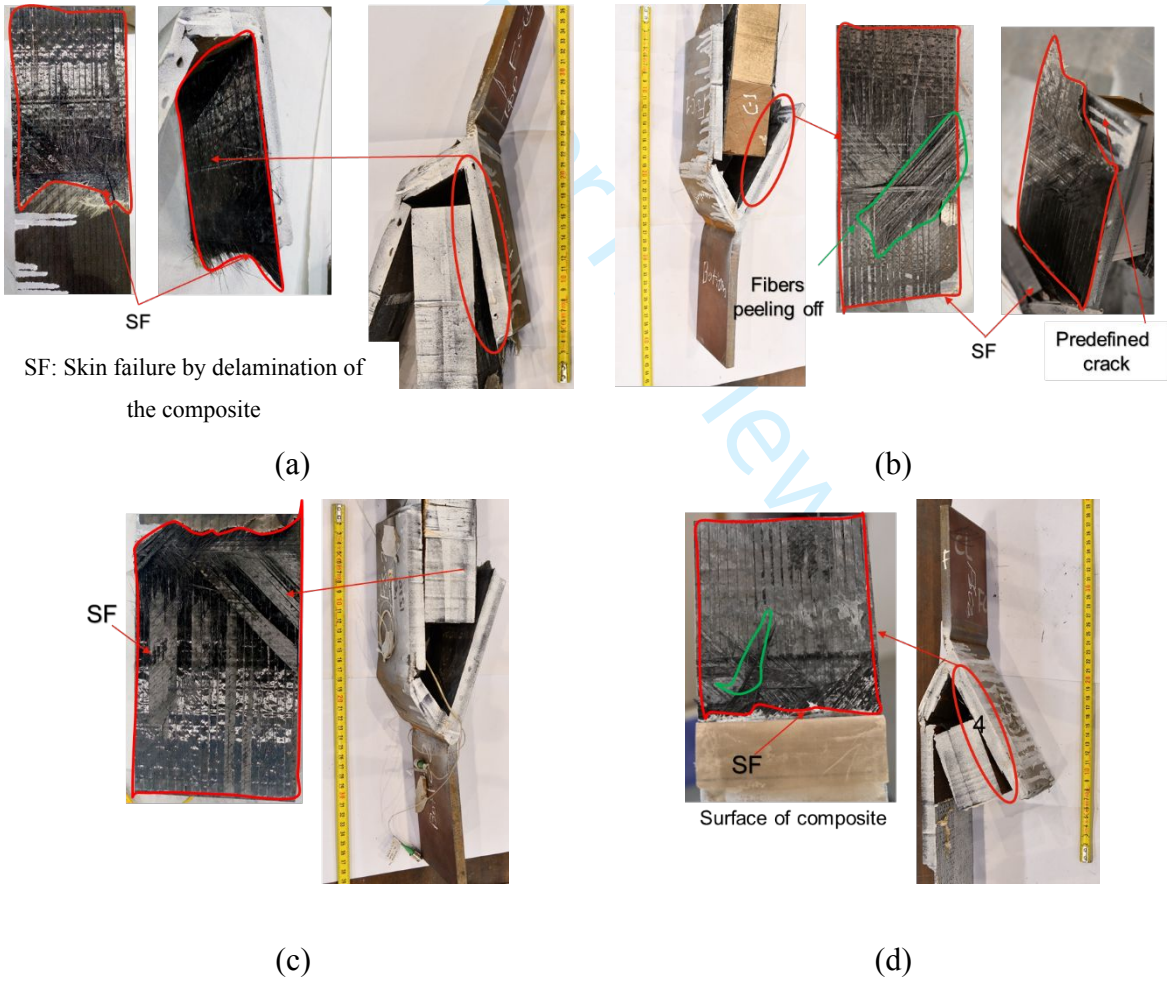


Figure 13 Failure modes of un-cracked (a) Fs-1 (c) Fs-2 and cracked (b) FsC-1 (d) FsC-2 large scale joint specimens.



## 6. Conclusions

This study addressed an experimental analysis of deformation and strain of large scale cracked and un-cracked multi-material joints. A sandwich panel of CFRP sheets and balsa core has been bonded to steel brackets using a thick layer of MMA adhesive. In two specimens, crack-like flaws were intentionally introduced at adhesive-composite and adhesive-steel interfaces. Both monotonic and stepwise loading tensile tests were performed, supported with DIC instrumentation and FBG sensors mounted on the front and back side of the steel brackets and composite panels of the specimen. The DIC technique was applied to measure strain at the surface of the bulk adhesive while strain at the external surface of the steel and composite was measured by FBG sensors. The following conclusions can be formulated.

- 1) DIC proved to be an effective method for characterising the evolution and distribution of local strain in the adhesive bond lines. The measured shear, longitudinal and peel strains reveal that the bond line of the joint was predominantly subjected to shear load. The bond lines at the free side of the cracked and un-cracked specimens showed an identical shear strain pattern with negligible strain magnitude. The shear, longitudinal and peel strain values are significantly higher (up to 96% higher) at the gripped side due to the asymmetrical design of the steel brackets. These findings can support future joint design improvements.
- 2) FBG sensors effectively measured the longitudinal strain responses at the front and back sides of the specimen. Based on this strain response, FBG instrumentation allows to detect the onset of damage in the adhesive bond line of the specimen. The load-longitudinal strain curves recorded by DIC inspection blocks placed in close proximity to FBG sensors showed a close correspondence with FBG measurements.

- 1
- 2
- 3) The un-cracked and cracked specimens showed sudden failure due to delamination of
- 4
- 5 the composite panel near the interface of adhesive and composite. The failure strength
- 6
- 7 of the cracked specimens was similar to the strength of the un-cracked specimens,
- 8
- 9 demonstrating the damage tolerance of the adhesive bonds.
- 10
- 11
- 12
- 13
- 14
- 15

16

17 **Funding:**

18

19

20 The authors acknowledge the following financial support for the research, authorship, and/or

21 publication of this article.

22

23

24

25

26 This research is carried out within the project "QUALIFY–Enabling Qualification of Hybrid

27 Joints for Lightweight and Safe Maritime Transport". This project received funding from the

28 Interreg2Seas Mers Zeeën programme 2014-2020 co-funded by the European Regional

29 Development Fund under subsidy contract No 03-051 and the province of East-Flanders.

30

31

32

33

34

35

36

37

38

39 **References:**

40

41

42

43 1. Weitzenböck JR, McGeorge D. Science and technology of bolt-adhesive joints. Adv

44 Struct Mater. 2011;6:177–99.

45

46

47 2. Boyd SW, Blake JIR, Sheno RA, Kapadia A. Integrity of hybrid steel-to-composite

48 joints for marine application. Proc Inst Mech Eng Part M J Eng Marit Environ.

49 2004;218(4):235–46.

50

51

52

53

54 3. Gupta V, Mohapatra PC, Smith L V. The effect of adhesive bondline thickness on joint

55 strength. In: CAMX Conference Proceedings Orlando, FL, October 13-16, 2014.

56

57 CAMX – The Composites and Advanced Materials Expo; 2014. p. 1–14.

58

59

60

4. Banea MD, Da Silva LFM, Campilho RDSG. The effect of adhesive thickness on the mechanical behavior of a structural polyurethane adhesive. *J Adhes.* 2014;91(5):331–46.
5. Zehsaz M, Vakili-Tahami F, Saeimi-Sadigh MA. Parametric study of the creep failure of double lap adhesively bonded joints. *Mater Des.* 2014;64(2014):520–6.
6. Liao L, Huang C, Sawa T. Effect of adhesive thickness, adhesive type and scarf angle on the mechanical properties of scarf adhesive joints. *Int J Solids Struct.* 2013;50(25–26):4333–40.
7. Huang J, Zeng J, Bai Y, Cheng Z, Wang Y, Zhao Q, et al. Effect of adhesive layer properties on the shear strength of single-lap structures of dissimilar materials based on the cohesive zone model. *J Mech Sci Technol.* 2021;35(1):133–43.
8. Fernández-Cañadas LM, Ivañez I, Sanchez-Saez S, Barbero EJ. Effect of adhesive thickness and overlap on the behavior of composite single-lap joints. *Mech Adv Mater Struct.* 2019;0(0):1–10.
9. da Silva LFM, Rodrigues TNSS, Figueiredo MAV, de Moura MFSF, Chousal JAG. Effect of adhesive type and thickness on the lap shear strength. *J Adhes.* 2006;82(11):1091–115.
10. Guo L, Liu J, Xia H, Li X, Zhang X, Yang H. Effects of surface treatment and adhesive thickness on the shear strength of precision bonded joints. *Polym Test.* 2021;94:107063.
11. Arenas JM, Narbón JJ, Alía C. Optimum adhesive thickness in structural adhesives joints using statistical techniques based on Weibull distribution. *Int J Adhes Adhes.* 2010;30(3):160–5.
12. Kim TH, Kweon JH, Choi JH. An experimental study on the effect of overlap length on

- the failure of composite-to-aluminum single-lap bonded joints. *J Reinf Plast Compos*. 2008;27(10):1071–81.
13. Özel A, Aydın MD, Temiz Ş. The effects of overlap length and adherend thickness on the strength of adhesively bonded joints subjected to bending moment. *J Adhes Sci Technol*. 2004;18(3):313–25.
14. Adams RD, Harris JA. The influence of local geometry on the strength of adhesive joints. *Int J Adhes Adhes*. 1987;7(2):69–80.
15. Kanani AY, Hou X, Laidlaw R, Ye J. The effect of joint configuration on the strength and stress distributions of dissimilar adhesively bonded joints. *Eng Struct*. 2021;226(July 2020):111322.
16. Lang TP, Mallick PK. Effect of spew geometry on stresses in single lap adhesive joints. *Int J Adhes Adhes*. 1998;18(3):167–77.
17. Moya-Sanz EM, Ivañez I, Garcia-Castillo SK. Effect of the geometry in the strength of single-lap adhesive joints of composite laminates under uniaxial tensile load. *Int J Adhes Adhes*. 2017;72(October 2016):23–9.
18. Papini M, Fernlund G, Spelt JK. The effect of geometry on the fracture of adhesive joints. *Int J Adhes Adhes*. 1994;14(1):5–13.
19. Sahin R, Akpınar S. The effects of adherend thickness on the fatigue strength of adhesively bonded single-lap joints. *Int J Adhes Adhes*. 2021;107(March):102845.
20. Zheng R, Lin J, Wang PC, Zhu C, Wu Y. Effect of adhesive characteristics on static strength of adhesive-bonded aluminum alloys. *Int J Adhes Adhes*. 2015;57:85–94.
21. Shi JW, Cao WH, Wu ZS. Effect of adhesive properties on the bond behaviour of externally bonded FRP-to-concrete joints. *Compos Part B Eng*. 2019;177(August):107365.

22. Hirulkar NS, Jaiswal PR, Alessandro P, Reis P. Influence of mechanical surface treatment on the strength of mixed adhesive joint. *Mater Today Proc.* 2018;5(9):18776–88.
23. Ghumatkar A, Budhe S, Sekhar R, Banea MD, De Barros S. Influence of adherend surface roughness on the adhesive bond strength. *Lat Am J Solids Struct.* 2016;13(13):2356–70.
24. Zhang D, Huang Y. Influence of surface roughness and bondline thickness on the bonding performance of epoxy adhesive joints on mild steel substrates. *Prog Org Coatings.* 2021;153(January):106135.
25. Russian O, Khan S, Belarbi A, Dawood M. Effect of surface preparation technique on bond behavior of CFRP-steel double-lap joints: Experimental and numerical studies. *Compos Struct.* 2021;255(September 2020):113048.
26. Spaggiari A, Dragoni E. Effect of mechanical surface treatment on the static strength of adhesive lap joints. *J Adhes.* 2013;89(9):677–96.
27. Katnam KB, Dhôte JX, Young TM. Experimental analysis of the bondline stress concentrations to characterize the influence of adhesive ductility on the composite single lap joint strength. *J Adhes.* 2013;89(6):486–506.
28. Da Silva LFM, Dillard DA, Blackman B, Adams RD. Testing adhesive joints, best practices. Lucas F.M. da Silva DAD, Bamber Blackman and RDA, editors. John Wiley & Sons; 2012.
29. Bagiatis V, Critchlow GW, Price D, Wang S, Harvey CM, Yuan B. Thermally induced strain in joints with dissimilar adherends bonded with a flexible adhesive. *Int J Adhes Adhes.* 2021;107:102853.
30. Vijaya Kumar RL, Bhat MR, Murthy CRL. Evaluation of kissing bond in composite

- adhesive lap joints using digital image correlation: Preliminary studies. *Int J Adhes Adhes*. 2013;42:60–8.
31. Sutton MA, Matta F, Rizos D, Ghorbani R, Rajan S, Mollenhauer DH, et al. Recent Progress in Digital Image Correlation: Background and Developments since the 2013 W M Murray Lecture. *Exp Mech*. 2017;57(1):1–30.
32. Broughton W. Testing the mechanical, thermal and chemical properties of adhesives for marine environments. *Adhes Mar Eng*. 2012;99–154.
33. Angelopoulos N. Damage detection and damage evolution monitoring of composite materials for naval applications using acoustic emission testing. The University of Birmingham; 2017.
34. Saleh MN, Saeedifar M, Zarouchas D, De Freitas ST. Stress analysis of double-lap bi-material joints bonded with thick adhesive. *Int J Adhes Adhes*. 2020;97(Mar 1):102480.
35. Askarinejad S, Martínez-Pañeda E, Cuesta II, Fleck N. Mode II fracture of an MMA adhesive layer: Theory versus experiment. *Eur J Mech A/Solids*. 2021;86(September 2020):1–9.
36. Thäsler T, Holtmannspötter J, Gudladt HJ. Monitoring the fatigue crack growth behavior of composite joints using in situ 2D-digital image correlation. *J Adhes*. 2019;95(5–7):595–613.
37. Jaiswal PR, Kumar RI, De Waele W. Unified methodology for characterisation of global fatigue damage evolution in adhesively bonded joints. *Frat ed Integrita Strutt*. 2020;14(53):26–37.
38. Da Silva LFM, Moreira PMGP, Loureiro ALD. Determination of the strain distribution in adhesive joints using Fiber Bragg Grating (FBG). *J Adhes Sci Technol*. 2014;28(14–

- 15):1480–99.
39. Ning X, Murayama H, Kageyama K, Wada D, Kanai M, Ohsawa I, et al. Dynamic strain distribution measurement and crack detection of an adhesive-bonded single-lap joint under cyclic loading using embedded FBG. *Smart Mater Struct.* 2014;23(10).
40. Xavier J, Fernandes JRA, Frazão O, Morais JJL. Measuring mode I cohesive law of wood bonded joints based on digital image correlation and fibre Bragg grating sensors. *Compos Struct.* 2015;121:83–9.
41. Saha S, Sullivan RW. Strain distributions in bonded composites using optical fibers and digital image correlation. *Proc Am Soc Compos - 34th Tech Conf ASC 2019.* 2019;(October).
42. Manterola J, Aguirre M, Zurbitu J, Renart J, Turon A, Urresti I. Using acoustic emissions ( AE ) to monitor mode I crack growth in bonded joints. 2020;224(2019).
43. Jaiswal PR, Kumar RI, Saeedifar M, Saleh MN, Luyckx G, De Waele W. Deformation and damage evolution of a full-scale adhesive joint between a steel bracket and a sandwich panel for naval application. *Proc Inst Mech Eng Part C J Mech Eng Sci.* 2020;
44. Clifford SM, Manger CIC, Clyne TW. Characterisation of a glass-fibre reinforced vinylester to steel joint for use between a naval GRP superstructure and a steel hull. *Compos Struct.* 2002;57(1–4):59–66.
45. Hildebrand M, Hentinen M. Efficient solutions for joints between large FRP-sandwich and metal structures. In: *Progress through innovation and cost effectiveness (Paris la Défense, 22-24 April 1998).* 1998. p. 417–28.
46. Elanchezhian C, Ramnath BV, Hemalatha J. Mechanical Behaviour of Glass and Carbon Fibre Reinforced Composites at Varying Strain Rates and Temperatures.



- Procedia Mater Sci. 2014;6:1405–18.
47. No . 47 Shipbuilding and repair quality standard (Rev. 7 June 2013). 2013.
48. Kaluza M, Hulimka J, Kubica J. Effectiveness of adhesive CFRP/steel joints Double-lap static tests. Brittle Matrix Compos 11 - Proc 11th Int Symp Brittle Matrix Compos BMC 2015. 2015;(September):479–88.
49. Kaluza M, Hulimka J. Methacrylate Adhesives to Create CFRP Laminate-steel Joints- Preliminary Static and Fatigue Tests. Procedia Eng. 2017;172:489–96.
50. Hulimka J, Kaluza M. Preliminary tests of steel-to-steel adhesive joints. Procedia Eng. 2017;172:385–92.
51. Banea MD, Rosioara M, Carbas RJC, da Silva LFM. Multi-material adhesive joints for automotive industry. Compos Part B Eng. 2018;151(March):71–7.
52. Jaiswal PR, Kumar RI, Saeedifar M, Saleh MN, Luyckx G, De Waele W. Deformation and damage evolution of a full-scale adhesive joint between a steel bracket and a sandwich panel for naval application. Proc Inst Mech Eng Part C J Mech Eng Sci. 2021;235(3):571–84.
53. Yang J, Wang W, Qiao L, Liu C. A Fiber Bragg Grating Sensor for Pressure Monitoring of Ship Structure Under Wave Load. In: International Conference in Communications, Signal Processing, and Systems. Springer; 2021. p. 159–66.
54. Tang H, Ren H, Jia L. Research on Applicability of Fiber Bragg Grating Sensor for Ship Structure Monitoring System. In: IOP Conference Series: Materials Science and Engineering. 2019.
55. Cao J, Grenestedt JL. Test of a redesigned glass-fiber reinforced vinyl ester to steel joint for use between a naval GRP superstructure and a steel hull. Compos Struct. 2003;60(4):439–45.

1  
2  
3  
4  
5  
6  
7  
8  
9  
10  
11  
12  
13  
14  
15  
16  
17  
18  
19  
20  
21  
22  
23  
24  
25  
26  
27  
28  
29  
30  
31  
32  
33  
34  
35  
36  
37  
38  
39  
40  
41  
42  
43  
44  
45  
46  
47  
48  
49  
50  
51  
52  
53  
54  
55  
56  
57  
58  
59  
60

For Peer Review

List of figures

Figure 1 Schematic illustration (a) and the actual appearance of fabricated large scale un-cracked (b) and cracked (c) adhesive joint (all dimensions in mm). .....2

*Figure 2 Schematic representation of tensile test setup, including DIC and DSLR camera.*.....3

Figure 3 Scheme for stepwise loading/unloading tensile test.....3

Figure 4 Mechanical behaviour of large scale specimens subjected to quasi-static tensile testing: (a) monotonically loaded, (b) stepwise loaded/unloaded.The circles refer to load levels used in the next figure. ....3

Figure 5 Shear strain ( $\epsilon_{xy}$ ) distributions at the lower joint of the un-cracked (Fs-1) and the cracked (FsC-1) specimens at different load levels during the quasi-static tensile test. ....4

Figure 6 Shear strain ( $\epsilon_{xy}$ ) distributions at the lower joint of the un-cracked (Fs-2) and the cracked (FsC-2) specimens at different load levels during the stepwise tensile test. ....5

Figure 7 Load versus local strain plots for six different regions at the adhesive surface of un-cracked (Fs-1; a,c,e) and cracked (FsC-1; b,d,f) specimens subjected to monotonic tensile load. *R0 to R5 refer to DIC inspection blocks.* .....6

Figure 8 Load versus local strain plots for six different regions at the adhesive surface of un-cracked (Fs-2; a,c,e) and cracked (FsC-2; b,d,f) specimens subjected to stepwise loading/unloading tensile load ( shear strain a,b; normal c,d; peel strain e,f). *R0 to R5 refer to DIC inspection blocks.* .....7

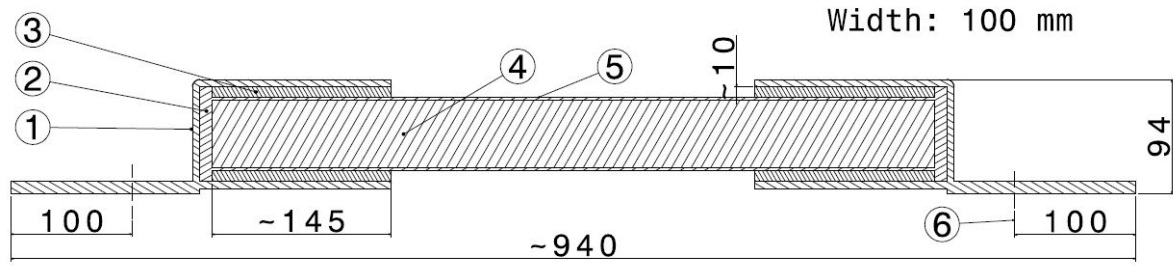
Figure 9 Location of (a) FBG sensors (red dots on the schematics) and (b) DIC inspection blocks. ....7

Figure 10 Load versus longitudinal strain curves for FBG sensors (a) S2-2, S3-2 and S31 , (b) S1 to S13 and S2 and (d) S14 to S26 and S2-3. ....8

Figure 11 Load versus longitudinal strain curve for FBG sensors and DIC inspection blocks placed on (a) composite and (b) steel.....8

Figure 12 Photographs illustrating global bending and sudden failure of an un-cracked specimen (Fs-1) at different load levels during the static tensile test.....9

Figure 13 Failure modes of un-cracked (a) Fs-1 (c) Fs-2 and cracked (b) FsC-1 (d) FsC-2 large scale joint specimens.....9

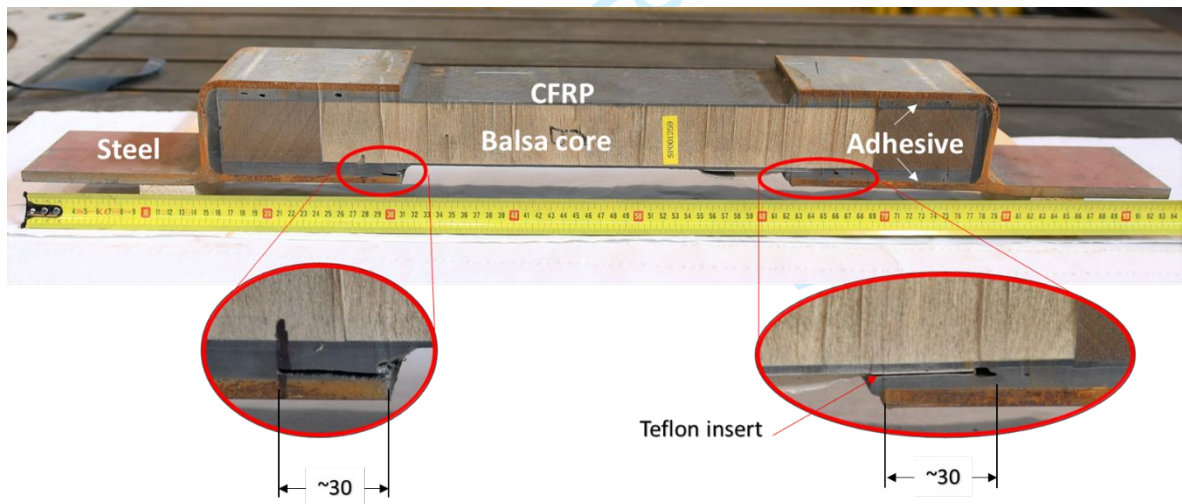


(a)

[1:Steel, 2:Foam, 3: Adhesive, 4: Balsa core, 5: Composite, 6: Grip length]



(b)



(c)

Figure 1 Schematic illustration (a) and the actual appearance of fabricated large scale un-cracked (b) and cracked (c) adhesive joint (all dimensions in mm).

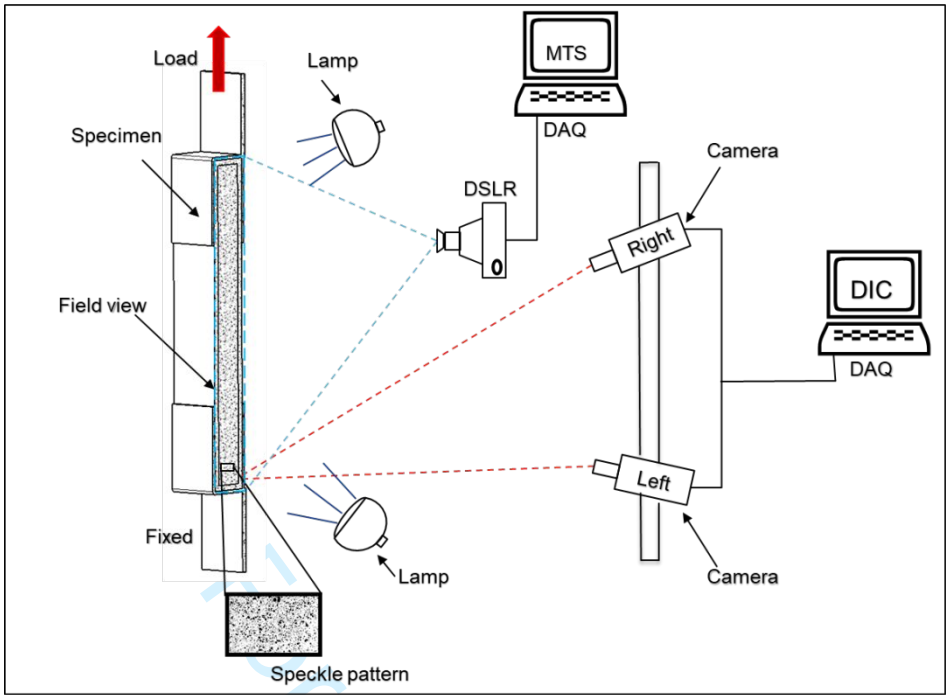


Figure 2 Schematic representation of tensile test setup, including DIC and DSLR camera.

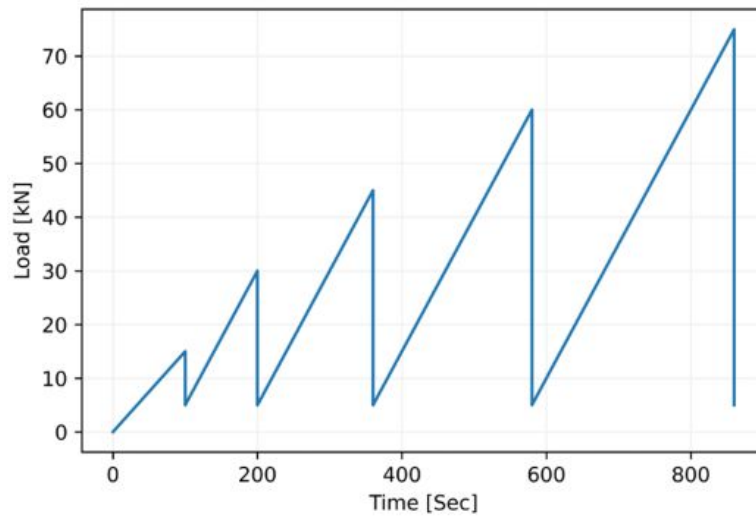


Figure 3 Scheme for stepwise loading/unloading tensile test.



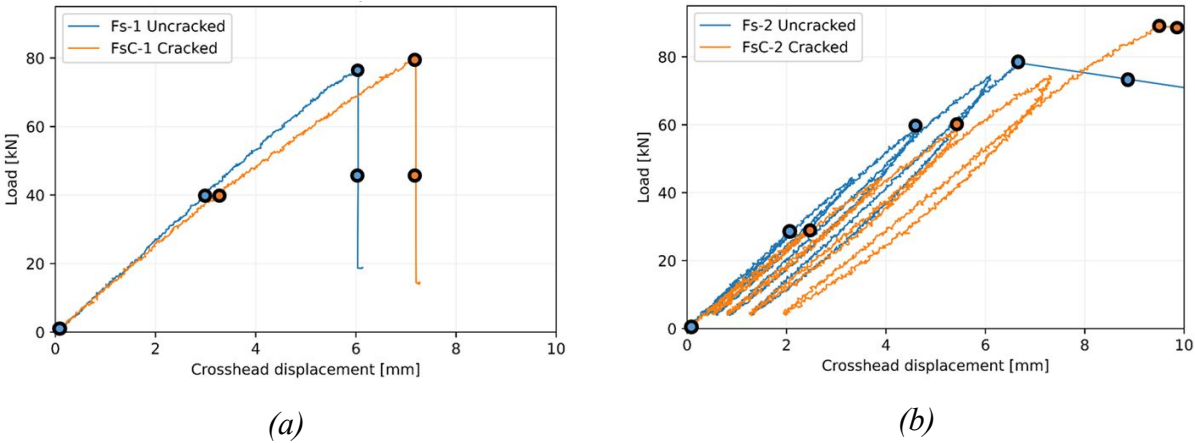


Figure 4 Mechanical behaviour of large scale specimens subjected to quasi-static tensile testing: (a) monotonically loaded, (b) stepwise loaded/unloaded. The circles refer to load levels used in the next figure.

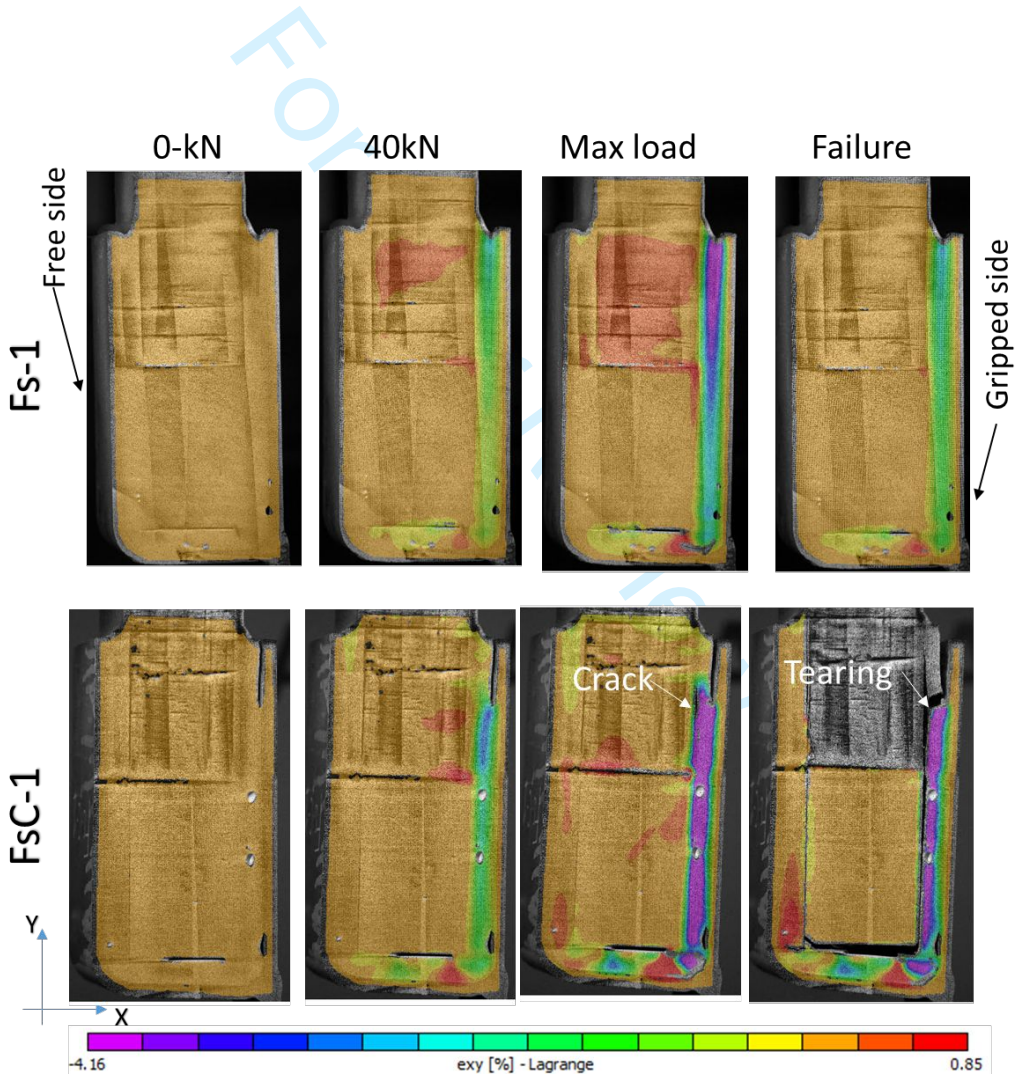


Figure 5 Shear strain ( $\epsilon_{xy}$ ) distributions at the lower joint of the un-cracked (Fs-1) and the cracked (FsC-1) specimens at different load levels during the quasi-static tensile test.

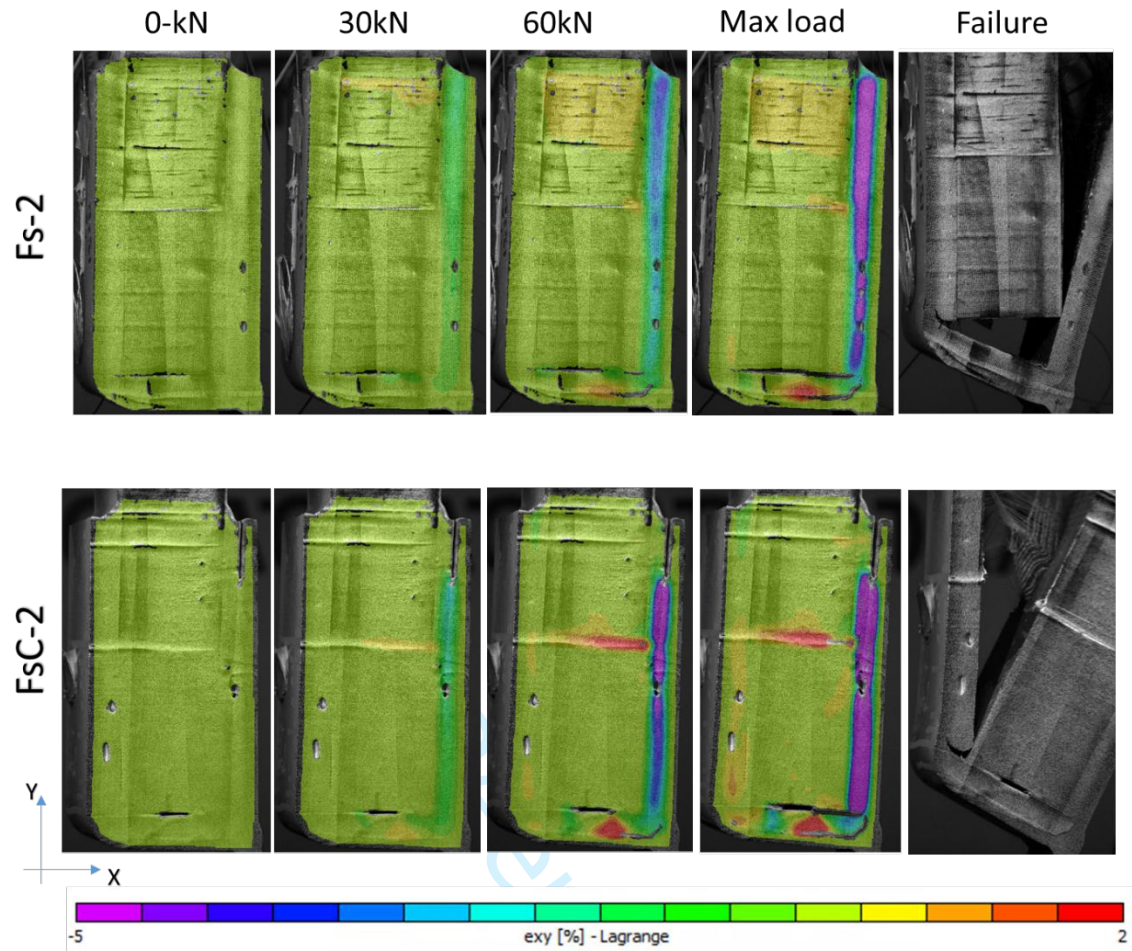
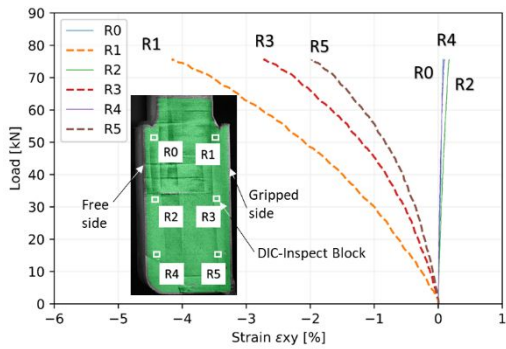
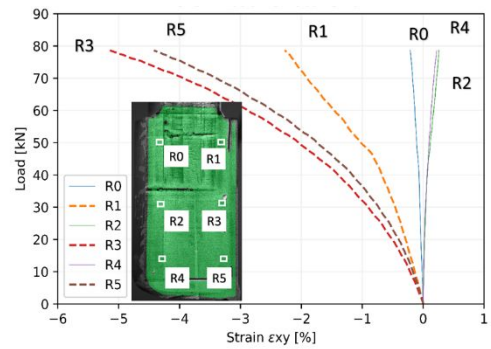


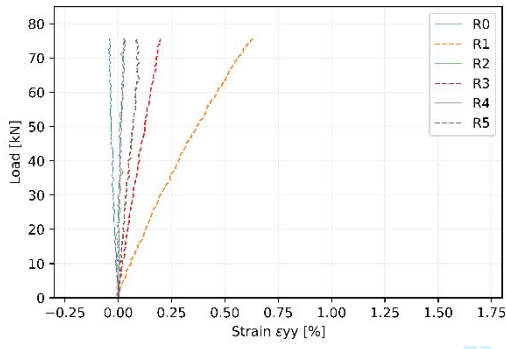
Figure 6 Shear strain ( $\epsilon_{xy}$ ) distributions at the lower joint of the un-cracked ( $Fs-2$ ) and the cracked ( $FsC-2$ ) specimens at different load levels during the stepwise tensile test.



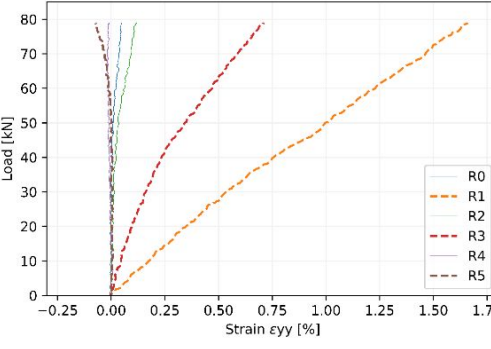
(a) shear strain



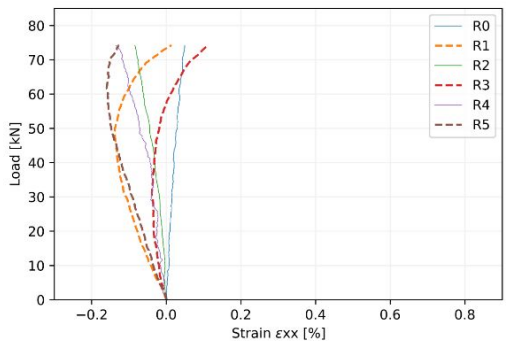
(b) shear strain



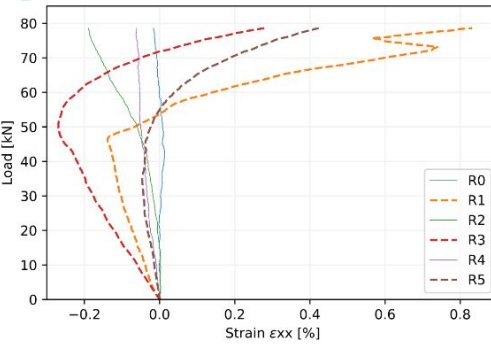
(c) longitudinal strain



(d) longitudinal strain



(e) peel strain



(f) peel strain

Figure 7 Load versus local strain plots for six different regions at the adhesive surface of un-cracked (Fs-1; a,c,e) and cracked (FsC-1; b,d,f) specimens subjected to monotonic tensile load. R0 to R5 refer to DIC inspection blocks.



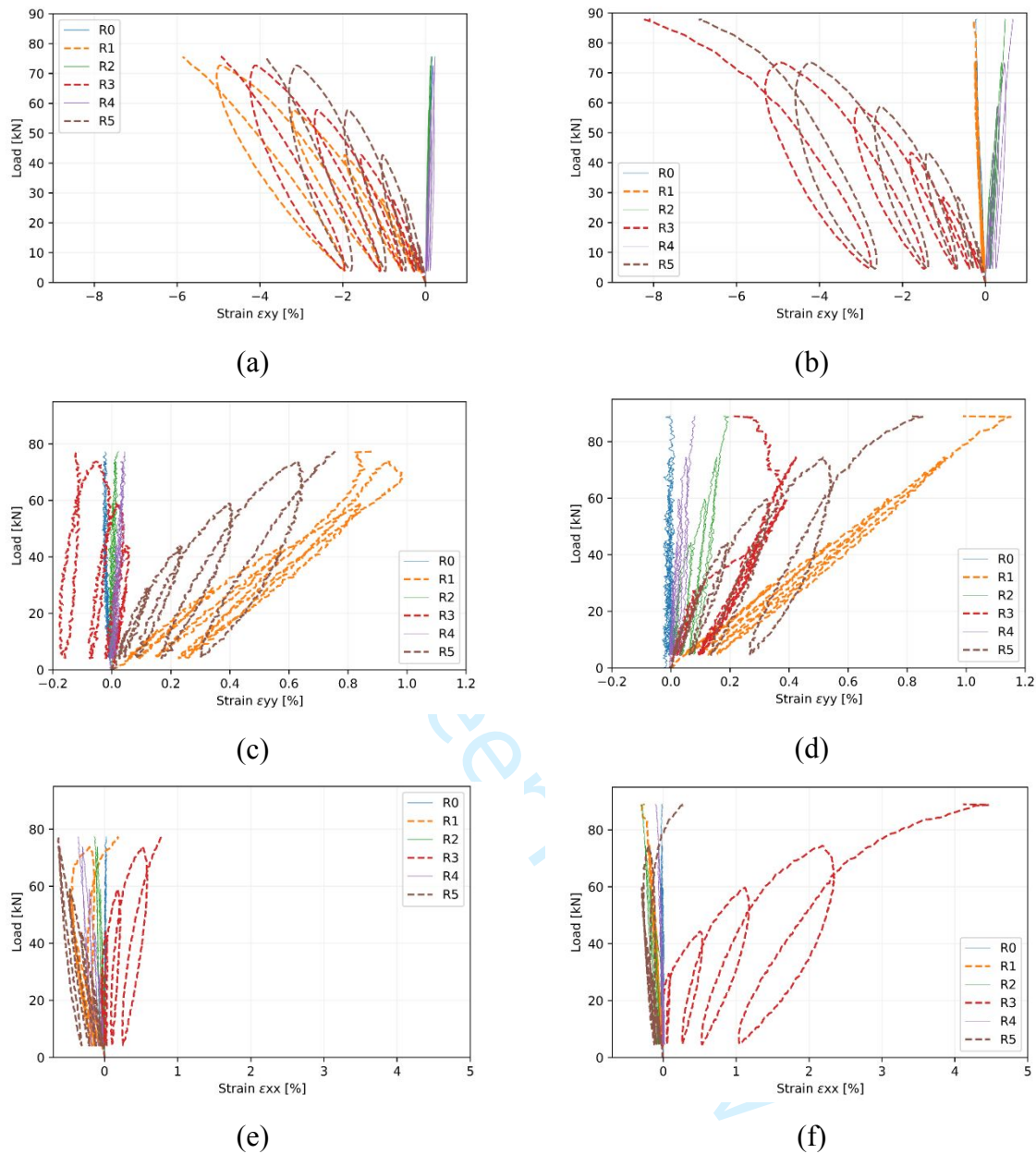
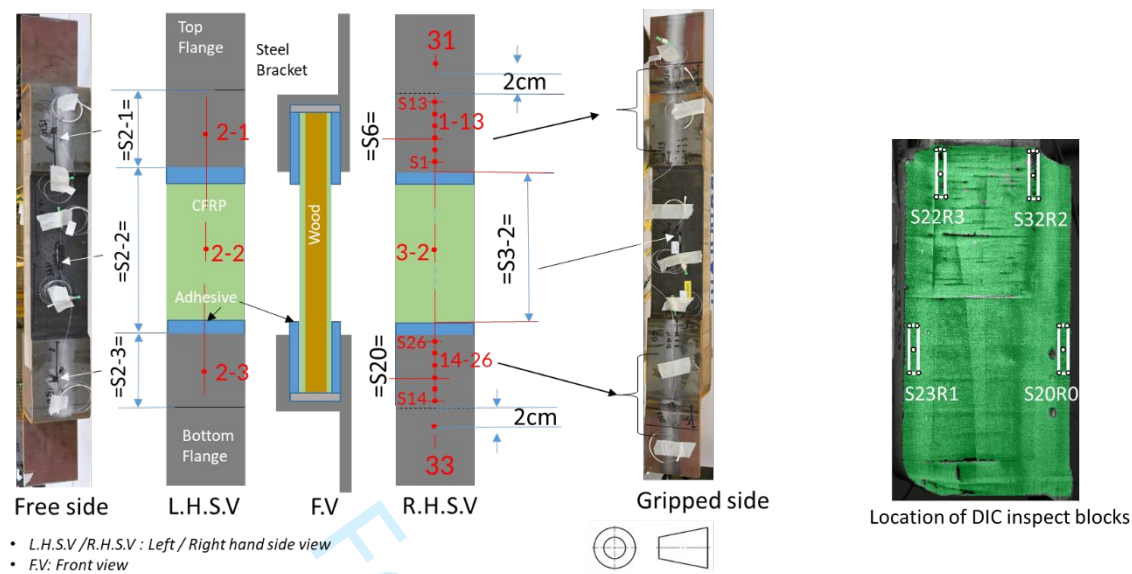


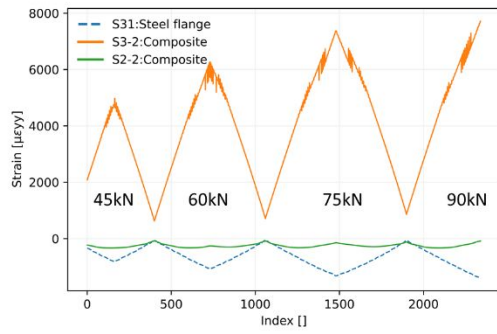
Figure 8 Load versus local strain plots for six different regions at the adhesive surface of un-cracked (Fs-2; a,c,e) and cracked (FsC-2; b,d,f) specimens subjected to stepwise loading/unloading tensile load ( shear strain a,b; normal c,d; peel strain e,f).

R0 to R5 refer to DIC inspection blocks.

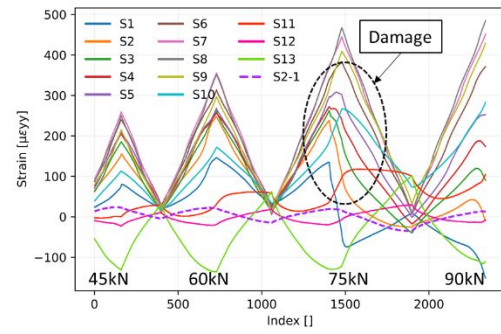


(b)

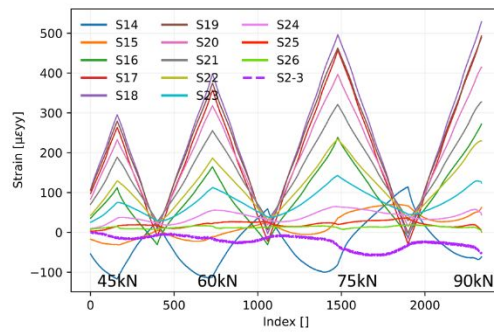
Figure 9 Location of (a) FBG sensors (red dots on the schematics) and (b) DIC inspection blocks.



(a) FBG sensors S2-2, S3-2 and S31.



(b) FBG sensors S1 to S13 and S2-1.



(c) FBG sensors S14 to S26 and S2-3.

Figure 10 Load versus longitudinal strain curves for FBG sensors (a) S2-2, S3-2 and S31 , (b) S1 to S13 and S2 and (d) S14 to S26 and S2-3.



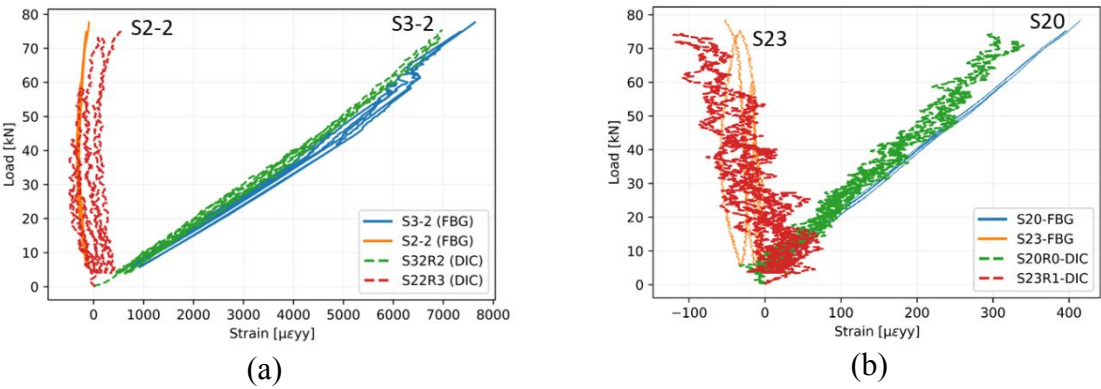


Figure 11 Load versus longitudinal strain curve for FBG sensors and DIC inspection blocks placed on (a) composite and (b) steel.

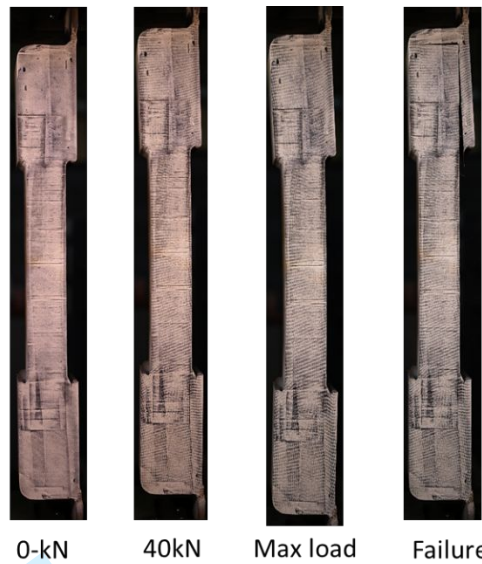


Figure 12 Photographs illustrating global bending and sudden failure of an un-cracked specimen (Fs-1) at different load levels during the static tensile test.

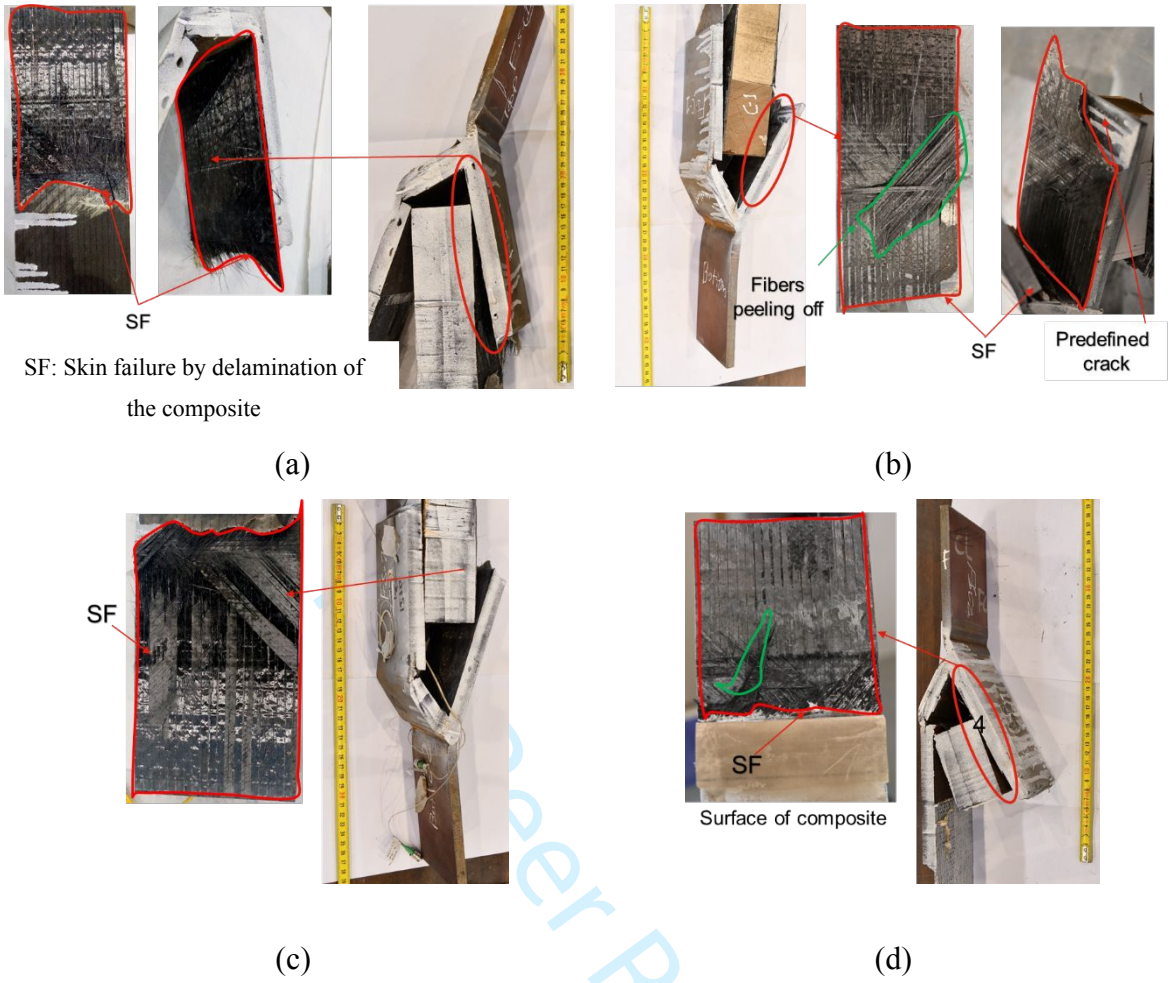


Figure 13 Failure modes of un-cracked (a) Fs-1 (c) Fs-2 and cracked (b) FsC-1 (d) FsC-2 large scale joint specimens.

## List of table

Table 1 Mechanical properties (37,52).....	2
--	---

For Peer Review

1  
2  
3  
4  
5  
6  
7  
8  
9  
10  
11  
12  
13  
14  
15  
16  
17  
18  
19  
20  
21  
22  
23  
24  
25  
26  
27  
28  
29  
30  
31  
32  
33  
34  
35  
36  
37  
38  
39  
40  
41  
42  
43  
44  
45  
46  
47  
48  
49  
50  
51  
52  
53  
54  
55  
56  
57  
58  
59  
60

Table 1 Mechanical properties (37,52).

	Steel AH-36	MMA adhesive	CFRP	Balsa
Tensile strength (MPa)	400-500	12-15	600-700	5-10
Yield stress (MPa)	355	-	(brittle failure)	
Young's modulus (GPa)	210	0.207-0.276	36	0.279
Poisson's ratio	0.26	-	0.32	
Lap shear strength (MPa)	-	16-19	-	
Shear modulus (GPa)	-	-	13.7	0.187

For Peer Review